



A holistic 3D finite element simulation model for thermoelectric power generator element



Guangxi Wu^a, Xiong Yu^{b,c,d,*}

^a Department of Electrical Engineering and Computer Science, Case Western Reserve University, Cleveland, OH 44106, USA

^b Department of Civil Engineering, Case Western Reserve University, Cleveland, OH 44106, USA

^c Department of Electrical Engineering and Computer Science (Courtesy Appointment), Case Western Reserve University, Cleveland, OH 44106, USA

^d Department of Mechanical and Aerospace Engineering (Courtesy Appointment), Case Western Reserve University, Cleveland, OH 44106, USA

ARTICLE INFO

Article history:

Received 15 February 2014

Accepted 12 April 2014

Available online 23 May 2014

Keywords:

Finite element simulation

Thermoelectric power generator

Effective Seebeck coefficient

Carrier density variation

ABSTRACT

Harvesting the thermal energy stored in the ambient environment provides a potential sustainable energy source. Thermoelectric power generators have advantages of having no moving parts, being durable, and light-weighted. These unique features are advantageous for many applications (i.e., carry-on medical devices, embedded infrastructure sensors, aerospace, transportation, etc.). To ensure the efficient applications of thermoelectric energy harvesting system, the behaviors of such systems need to be fully understood. Finite element simulations provide important tools for such purpose. Although modeling the performance of thermoelectric modules has been conducted by many researchers, due to the complexity in solving the coupled problem, the influences of the effective Seebeck coefficient and carrier density variations on the performance of thermoelectric system are generally neglected. This results in an over-estimation of the power generator performance under strong-ionization temperature region. This paper presents an advanced simulation model for thermoelectric elements that considers the effects of both factors. The mathematical basis of this model is firstly presented. Finite element simulations are then implemented on a thermoelectric power generator unit. The characteristics of the thermoelectric power generator and their relationship to its performance are discussed under different working temperature regions. The internal physics processes of the TEM harvester are analyzed from the results of computational simulations. The new model presented by this paper is more conservative than the traditional model in predicting the performance of TEM power generator working under strong-ionization region. By accounting for the mechanisms that are typically ignored or simplified in the existing models, this new model provides more holistic descriptions on the thermoelectric power generator behaviors and therefore potentially will further improve the accuracy in the computational simulations.

© 2014 Elsevier Ltd. All rights reserved.

1. Introduction

Thermoelectric module (TEM) converts thermal and electrical energy with no moving parts. It is light-weighted and durable. When serving as a power source, TEM generates electric power through utilizing thermal energy and is usually called thermoelectric generator (TEG). It has been employed as power sources in wristwatches [1], satellites, space probes, and unmanned remote facilities. Thermoelectric module is also promising to provide innovative solutions for energy applications in transportation arena. These include, for example, harvesting the waste heat from vehicle engine and exhaust gas [2], utilizing the thermal energy contained

in pavement [3] and other infrastructure to provide electricity supplies for sensors, etc. Design and optimization of TEM performance relies on understanding the materials properties and fundamental energy conversion mechanism.

Analytic models have been developed to describe the behaviors and performances of thermoelectric devices. To obtain analytic solutions, simplifications have to be made, i.e., the Thomson effects and temperature dependency of material properties are generally neglected [4–8]. There are also efforts in refining the models to include the Thomson effects [9] and the temperature dependency of material properties [10–12]. However, there are inherent limitations of analytical method due to its incapability to account for complex processes and materials properties.

Models based on electrical analogy method utilizes the mature knowledge in the area of electric circuits for thermal field analysis [13,14]. Finite difference software SPICE (Simulation Program with

* Corresponding author at: Department of Civil Engineering, Case Western Reserve University, Cleveland, OH 44106, USA.

E-mail addresses: gwxw94@case.edu (G. Wu), xxxy21@case.edu (X. Yu).

Nomenclature

TEM	thermoelectric module
TEG	thermoelectric generator
\mathbf{J}	electric current per unit area (A/m^2)
$\mathbf{J}_{\text{drift}}$	drift current (A/m^2)
$\mathbf{J}_{\text{diffusion}}$	diffusion current (A/m^2)
\mathbf{q}	heat transfer rate per unit area (W/m^2)
\mathbf{n}	outward unit normal vector
V	electrostatic potential (V)
T	temperature (K)
T_{top}	top boundary temperature (K)
T_{bottom}	bottom boundary temperature (K)
C_m	heat capacity ($\text{J}/(\text{K kg})$)
e	unit charge (C)
n	free electron density (m^{-3})
p	free hole density (m^{-3})
k_0	Boltzmann constant (J/K)
h	Planck constant (J s)
E_F	Fermi level (eV)
E_C	bottom edge of the conduction band (eV)
E_V	top edge of the valence band (eV)
E_D	energy level for donors (eV)
E_A	energy level for acceptors (eV)
N_C	effective density of states in conduction band (m^{-3})
N_V	effective density of states in the valence band (m^{-3})
N_D	donor impurity concentration (m^{-3})
N_A	acceptor impurity concentration (m^{-3})
m_n^*	electron effective mass (kg)
m_p^*	hole effective mass (kg)
m_0	electron rest mass (kg)
D	carrier diffusion coefficient (m^2/s)

Greek letters

σ	electrical conductivity (S/m)
α	Seebeck coefficient (V/K)
$\tilde{\alpha}$	effective Seebeck coefficient (V/K)
$\delta\alpha$	delta Seebeck coefficient (V/K)
κ	thermal conductivity at zero current ($\text{W}/(\text{m K})$)
κ_c	convective heat transfer coefficient ($\text{W}/(\text{m}^2 \text{K})$)
ρ	electrical resistivity (Ωm)
ρ_m	material density (kg/m^3)
$\bar{\mu}$	electrochemical potential (eV)
μ	chemical potential (eV)
τ	Thomson coefficient (V/K)

Subscripts

<i>drift</i>	drift
<i>diffusion</i>	diffusion
<i>bottom</i>	bottom edge
<i>top</i>	top edge
<i>m</i>	material
<i>c</i>	convective
<i>C</i>	conduction band
<i>F</i>	Fermi
<i>V</i>	valence band
<i>D</i>	donors
<i>A</i>	acceptors
<i>n</i>	electron
<i>p</i>	hole
<i>0</i>	constant

Integrated Circuit Emphasis), which is widely used in the area of circuit analysis, has been used for modeling the thermoelectric harvesters [15–19]. The advantage of this approach is that the thermal field and electric field can be easily coupled in the same simulation environment. While this method is powerful in simulating complex circuit loads connected to the thermoelectric power generator, use of such tools requires specialized training. This can pose significant limits on its applications. The electrical abstraction of the thermoelectric device typically focuses on the influence of the macroscopic performance of the TEM, such as the output power, and temperature difference between the two ends. Parameter distributions (especially three dimensional distributions) inside the TEM are difficult to be visualized with electrical analogy method. This method lacks the sensitivity of the module size on the TEM performance, which makes it difficult to optimize the shape of the TEM. In order to increase the visualization ability of the electrical analogy method, a three dimensional TCAD (Synopsys Technology Computer Aided Design) implementations have been conducted [20–23]. However, the governing equations and the performances of the TEM model still need to be further verified.

With the advancement in its multi-physics simulation capability, the finite element method (FEM) has become an attractive method to simulate the TEM performance numerically [24–29]. Thomson effects and temperature dependent properties of the TEM materials are easily coupled into the governing equations [30–32]. The finite element method features the advantages of user-friendly interface for model construction and results visualization as well as accuracy in the simulation results [33]. The multi-physics simulation capability helps to couple the interactions between the thermal, electrical, as well as other physics fields such as the mechanical field [34,35].

The current density equation used by these previous finite element models can be summarized as Eq. (1). Eq. (1) does not consider the effects of chemical potential on the properties of thermoelectric materials, which however has been found to have major impacts on the thermoelectric conversion. The chemical potential can be induced through using the effective Seebeck coefficient, which will be introduced in details in the subsequent context of this paper.

$$\mathbf{J} = -\sigma \cdot (\nabla V + \alpha \cdot \nabla T) \quad (1)$$

where the vector \mathbf{J} is the electric current per unit area; σ is the electrical conductivity; V is the electrostatic potential; α is Seebeck coefficient and T is the temperature.

Besides, Eq. (1) is only applicable for homogeneous conditions, where carrier density is uniform in the semiconductor materials that form the legs of TEM. However, TEM has different temperatures at two ends under operation conditions in order to form the thermal gradient. Correspondingly, carrier (electrons or holes) densities are different at the two ends under non-strong-ionization regions (including low-temperature weak-ionization region and high-temperature intrinsic-ionization region, etc.) due to the differences in the excitation energies under different temperatures. This will drive carriers to diffuse along the density gradient. Mahan [36] pointed out that the density always varies as long as there is a current flowing in the leg and only by introducing variations in the particle density can we eliminate the violation of Poisson's equation under homogeneous conditions.

This paper describes an improved model for TEM that considers the effects of chemical potential and carrier density variations. We firstly derive the general governing equations and auxiliary relationships that describe the physical processes in TEM, using n-type

semiconductor material as an example. Chemical potential (i.e., the effective Seebeck coefficient) is discussed under homogeneous condition and carrier density variation is considered under inhomogeneous condition. The equation system is solved with finite element platform COMSOL for a typical thermoelectric generator unit. The characteristics and performances of the module are discussed.

2. Governing equations

The equations governing the multi-dimensional temperature and electrical potential distributions in thermoelectric material are the energy conservation equation and charge conservation equations [37] in the absence of an applied magnetic field.

$$\rho_m C_m \frac{\partial T}{\partial t} = \nabla(\kappa \nabla T) + \rho \mathbf{J}^2 - \mathbf{TJ} \left[\left(\frac{\partial \alpha}{\partial T} \right) \nabla T + (\nabla \alpha)_T \right] \quad (2)$$

$$\nabla \cdot \mathbf{J} = 0 \quad (3)$$

where

$$\mathbf{J} = -\sigma \left[\nabla \left(\frac{\mu}{e} \right) + \alpha \nabla T \right] = -\sigma \left[\nabla \left(\frac{\mu}{e} + V \right) + \alpha \nabla T \right] \quad (4)$$

$$\mathbf{q} = \alpha \mathbf{TJ} - \kappa \nabla T \quad (5)$$

Here the vector \mathbf{J} is the electric current per unit area; the vector \mathbf{q} is the heat transfer rate per unit area; C_m is the heat capacity with unit of J/(K kg); ρ_m is the material density with unit of kg/m³; T is the temperature; κ is the thermal conductivity at zero current; $\sigma = 1/\rho$ is the electrical conductivity; ρ is the electrical resistivity; α is the Seebeck coefficient; $\bar{\mu} = \mu + eV$ is the electrochemical potential; μ is the chemical potential; V is the electrostatic potential; and e is the unit charge of charged particles giving rise to the electrical current, which is positive for hole and negative for electron. All material properties (α , κ , σ , etc.) are functions of temperature. The Seebeck coefficient can also be dependent on other factors, such as doping, besides temperature. However, they are neglected for simplicity in this paper.

The last term of Eq. (2) includes both Peltier effect and Thomson effect. Peltier effect describes heat absorbed by the junction from the environment and is calculated as the term $\mathbf{TJ}(\nabla \alpha)_T$. At the junction interface, where two different materials are in contact, temperature is the same across the junction because of heat exchange. Heat absorption is due to the differences in the Seebeck coefficients of junction materials. Inside the TEM element where thermoelectric material remains the same, Peltier heat equals to zero.

Thomson effect is represented by the term $\mathbf{TJ} \left(\frac{\partial \alpha}{\partial T} \right) \nabla T = \tau \mathbf{J} \nabla T$, where τ is the Thomson coefficient. The Thomson effect is caused by the Seebeck coefficient gradient which results from the temperature gradient along the thermoelectric material.

The sign in front of the term $\mathbf{TJ} \left[\left(\frac{\partial \alpha}{\partial T} \right) \nabla T + (\nabla \alpha)_T \right]$ of Eq. (2) is dependent on the sign convention of Thomson coefficient. Under the convention that the Thomson coefficient τ is considered to be positive if the conductor tends to become cooler (or heat is released) when the current flows in the direction of the positive temperature gradient [38], the sign of the last term is negative. Under the opposite convention where $\tau > 0$ implies that heat is absorbed when current flows towards regions of higher temperature [6], the sign in front of the last term is positive. Generally the former convention is used by most researchers.

The chemical potential μ is a function of particle density and the temperature T [39].

$$\nabla \mu = \left(\frac{\partial \mu}{\partial n} \right)_T \cdot \nabla n + \left(\frac{\partial \mu}{\partial T} \right)_n \cdot \nabla T \quad (6)$$

Plugging Eq. (6) into (4), we have

$$\mathbf{J} = -\sigma \cdot \nabla V - \sigma \alpha \cdot \nabla T - \sigma \left(\frac{\partial \mu}{e \partial T} \right)_n \nabla T - \sigma \left(\frac{\partial \mu}{e \partial n} \right)_T \nabla n \quad (7)$$

2.1. Effective Seebeck coefficient

Similar to the second term in Eq. (7), the third term also corresponds to electrical conductivity σ and temperature gradient ∇T . In other words, the factor $\left(\frac{\partial \mu}{e \partial T} \right)_n$ plays a role on the Seebeck coefficient, which is included in the term of effective Seebeck coefficient as in Eq. (8) [36].

$$\bar{\alpha} = \alpha + \left(\frac{\partial \mu}{e \partial T} \right)_n \equiv \alpha + \delta \alpha \quad (8)$$

where term $\left(\frac{\partial \mu}{e \partial T} \right)_n$ is defined as the delta Seebeck coefficient. Then Eq. (7) becomes

$$\mathbf{J} = -\sigma \cdot \nabla V - \sigma \bar{\alpha} \cdot \nabla T - \sigma \left(\frac{\partial \mu}{e \partial n} \right)_T \nabla n \quad (9)$$

The effective Seebeck coefficient contains the derivative of the chemical potential with respect to the temperature, as well as the delta Seebeck coefficient. For n-type semiconductor material, the chemical potential μ is equal to the difference between the Fermi energy level E_F and the bottom edge of the conduction band E_C [6].

$$\mu = E_F - E_C \quad (10)$$

Assuming that E_C is not dependent on temperature, there is

$$\delta \alpha = \left(\frac{\partial \mu}{e \partial T} \right)_n = \left[\frac{\partial(E_F - E_C)}{e \partial T} \right]_n = \left(\frac{\partial E_F}{e \partial T} \right)_n \quad (11)$$

From theories of semiconductor physics, the following expression of Fermi energy level is obtained following the Maxwell-Boltzmann statistics for n-type material under different ionization regions corresponding to different temperature levels [40].

Low-temperature weak-ionization region :

$$E_F = \frac{E_C + E_D}{2} + \frac{k_0 T}{2} \ln \left(\frac{N_D}{2N_C} \right) \quad (12)$$

Room-temperature strong-ionization region :

$$E_F = E_C + k_0 T \ln \left(\frac{N_D}{N_C} \right) \quad (13)$$

High-temperature intrinsic-ionization region :

$$E_F = \frac{E_C + E_V}{2} + \frac{k_0 T}{2} \ln \left(\frac{N_V}{N_C} \right) \quad (14)$$

where k_0 is the Boltzmann constant and equals to 1.38×10^{-23} J/K; E_D is the energy level for donors; E_V is the top edge of the valence band; N_D is the donor impurity concentration; N_V is the effective density of states in the valence band; N_C is the effective density of states in conduction band and can be described as follows:

$$N_C = 2 \frac{(2\pi m_n^* k_0 T)^{\frac{3}{2}}}{h^3} \quad (15)$$

$$N_V = 2 \frac{(2\pi m_p^* k_0 T)^{\frac{3}{2}}}{h^3} \quad (16)$$

where m_n^* and m_p^* are the electron effective mass and hole effective mass, respectively; h is Planck constant.

Assuming E_D , E_C , E_V , N_D , m_n^* and m_p^* are independent of temperature and plugging Eqs. (12)–(16) into (11), we can get the results of delta Seebeck coefficient as follows:

$$\text{Weak-ionization region : } \delta\alpha = \frac{k_0}{2e} \left[\ln \left(\frac{N_D}{2N_C} \right) - \frac{3}{2} \right] \quad (17)$$

$$\text{Strong-ionization region : } \delta\alpha = \frac{k_0}{e} \left[\ln \left(\frac{N_D}{N_C} \right) - \frac{3}{2} \right] \quad (18)$$

$$\text{Intrinsic-ionization region : } \delta\alpha = \frac{3k_0}{4e} \ln \left(\frac{m_p^*}{m_n^*} \right) \quad (19)$$

From Eqs. (15)–(19), for the weak and strong-ionization regions, the delta Seebeck coefficient depends on the donor impurity concentration (N_D), the electron effective mass (m_n^*), and the temperature. The relationships can be referred to Fig. 1 using the strong-ionization region as an example.

Fig. 1 shows that the delta Seebeck coefficient $\delta\alpha$ is positive for n-type material under strong-ionization region because the donor impurity concentration N_D is less than the effective density of states in conduction band N_C and e is negative (referring to Eq. (18)). Usually the Seebeck coefficient α is negative for n-type material. Therefore, the signs of $\delta\alpha$ and α are opposite under strong-ionization region, which is also true for weak-ionization region of both n-type and p-type material, as well as strong-ionization region of p-type material.

For the intrinsic-ionization region in the case of n-type material, $\delta\alpha$ changes as the ratio between the hole effective mass (m_p^*) and electron effective mass (m_n^*) changes. m_p^* and m_n^* can be calculated according to the corresponding band structure of the thermoelectric semiconductor material. When $m_p^* < m_n^*$, $\delta\alpha$ has an opposite sign of α . When $m_p^* > m_n^*$, $\delta\alpha$ has the same sign of α . For p-type material, the delta Seebeck coefficient $\delta\alpha$ is the same as n-type material. Therefore, when $m_p^* < m_n^*$, $\delta\alpha$ has the same sign as α ; when $m_p^* > m_n^*$, $\delta\alpha$ has an opposite sign of α .

Besides, the Seebeck coefficient of the most used thermoelectric power generator material is of several hundreds of micro-volts per Kelvin ($\mu\text{V/K}$). It can also be seen from the figure that the absolute value of $\delta\alpha$ is comparable to α , especially for material with high effective electron mass (m_n^*) under low doping level. This results in a significant influence of the effective Seebeck coefficient, as

well as the current caused by temperature gradient (referring to Eq. (9)). Therefore, this factor should not be neglected as Mahan [36] pointed out. The effective Seebeck coefficient is considered in the model implemented in this paper.

With the calculation of the delta Seebeck coefficient and the effective Seebeck coefficient, we can calculate the current driven by temperature gradient via Eq. (9). Actually, the temperature gradient leads to a voltage potential gradient in TEM through effective Seebeck coefficient. Therefore current driven by temperature gradient and potential gradient can be included as drift current as follows:

$$\mathbf{J}_{\text{drift}} = -\sigma \cdot \nabla V - \sigma \tilde{\alpha} \cdot \nabla T \quad (20)$$

2.2. Carrier density variation

The last term $\sigma \left(\frac{\partial \mu}{\partial n} \right)_T \nabla n$ in Eqs. (7) or (9) describes diffusion current introduced by carrier density gradient in the semiconductor thermoelectric material. Usually in semiconductor physics, the relationship between the diffusion current density and carrier density gradient is connected through the carrier diffusion coefficient, following Eq. (21).

$$\mathbf{J}_{\text{diffusion}} = -eD \cdot \nabla n \quad (21)$$

Comparing Eq. (21) with term $\sigma \left(\frac{\partial \mu}{\partial n} \right)_T \nabla n$, we can derive the expression of D :

$$D = \frac{\sigma}{e^2} \left(\frac{\partial \mu}{\partial n} \right)_T = \frac{\sigma}{e^2} \left[\frac{\partial (E_F - E_C)}{\partial n} \right]_T \quad (22)$$

In n-type semiconductor material, the density of carrier electrons is:

$$n = N_C \exp \left(-\frac{E_C - E_F}{k_0 T} \right) \quad (23)$$

The derivative in Eq. (22) is shown in Eq. (24) under the assumption that N_C is independent of n :

$$\frac{\partial (E_F - E_C)}{\partial n} = \frac{k_0 T}{n} \quad (24)$$

Plugging Eq. (24) into (22), we have

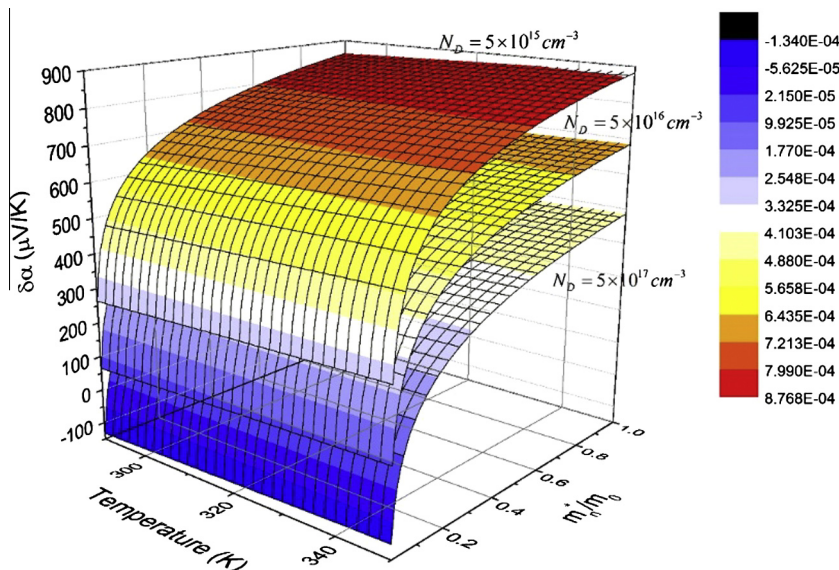


Fig. 1. The relationship between the delta Seebeck coefficient and the donor impurity concentration (N_D), the relative electron effective mass (m_n^*/m_0) and the temperature under the strong-ionization region for n-type thermoelectric material, where m_0 is the electron rest mass.

$$D = \frac{\sigma}{e^2} \left(\frac{\partial \mu}{\partial n} \right)_T = \frac{\sigma k_0 T}{e^2 n} \quad (25)$$

The total current can be calculated from the derived the expressions of drift current and diffusion current:

$$\begin{aligned} \mathbf{J} &= \mathbf{J}_{\text{drift}} + \mathbf{J}_{\text{diffusion}} \\ \mathbf{J}_{\text{drift}} &= -\sigma \cdot \nabla V - \sigma \tilde{\alpha} \cdot \nabla T \\ \mathbf{J}_{\text{diffusion}} &= -eD \cdot \nabla n \end{aligned} \quad (26)$$

Eq. (26) reveals the nature of current flowing inside the thermoelectric material. It is made up by drift current and diffusion current. The drift current is driven by the electric field governed by the gradient of electric potential and effective Seebeck potential. The diffusion current is caused by the variations in the carrier concentration and is usually neglected by most current models in the published literature. The model developed in this paper is an improvement over existing models by considering the effects of both drift currents and diffusion currents.

IN SUMMARY, the governing equations and auxiliary equations for the holistic computational model of TEM are listed in the following:

$$\text{Governing equations: } \begin{cases} \rho_m C_m \frac{\partial T}{\partial t} = \nabla(\kappa \nabla T) + \rho \mathbf{J}^2 - \mathbf{T} \mathbf{J} \left[\left(\frac{\partial \alpha}{\partial T} \right) \nabla T + (\nabla \alpha)_T \right] \\ \mathbf{J} = -\sigma \cdot \nabla V - \sigma \tilde{\alpha} \cdot \nabla T - eD \cdot \nabla n \\ \mathbf{J} = -\sigma \cdot \nabla V - \sigma \tilde{\alpha} \cdot \nabla T - eD \cdot \nabla p \\ \nabla \cdot \mathbf{J} = 0 \\ \mathbf{q} = \alpha \mathbf{T} \mathbf{J} - \kappa \nabla T \end{cases} \quad (27)$$

$$\text{Auxiliary equations: } \begin{cases} \text{n-type material} & \text{p-type material} \\ N_C = 2 \left(\frac{2\pi m_n^* k_0 T}{h^3} \right)^{\frac{3}{2}} & N_V = 2 \left(\frac{2\pi m_p^* k_0 T}{h^3} \right)^{\frac{3}{2}} \\ n = N_C \exp \left(-\frac{E_C - E_F}{k_0 T} \right) & p = N_V \exp \left(\frac{E_V - E_F}{k_0 T} \right) \\ D_n = \frac{\sigma k_0 T}{e^2 n} & D_p = \frac{\sigma k_0 T}{e^2 p} \\ \tilde{\alpha} = \alpha + \delta \alpha & \tilde{\alpha} = \alpha + \delta \alpha \\ \delta \alpha = \left[\frac{\partial(E_F - E_C)}{e \partial T} \right]_n & \delta \alpha = \left[\frac{\partial(E_V - E_F)}{e \partial T} \right]_p \end{cases} \quad (28)$$

where N_V is the effective density of states in valance band. E_F and $\delta \alpha$ can be referred to Table 1 corresponding to different temperature levels.

2.3. Homogeneous and inhomogeneous conditions

For strong-ionization region, if we plug Eq. (13) into (23), we can get the carrier concentration of electrons as

$$n = N_D \quad (29)$$

When the semiconductor thermoelectric material is evenly doped with impurities, the carrier concentration inside the material keeps as a constant everywhere when temperature changes

and is entirely contributed by the ionization of doped impurity. Therefore the diffusion current (Eq. (21)) is zero. This scenario can be seen as the so-called homogeneous case, which can be applied to TEMs used in the room temperature range.

If the semiconductor thermoelectric material is doped in gradient, or working under weak-ionization region and intrinsic-ionization region even though doped evenly, the previous phenomenon of uniform carrier concentration does not happen. Carrier concentration increases dramatically as temperature increases. In such inhomogeneous scenarios, the diffusion current arouses and is driven by the carrier concentration gradient. TEM applications under low-temperature range (for example, outer space applications) and high-temperature range (for example, thermal power plant applications) follow these phenomena.

Fig. 2 gives the schematic of carrier concentration variations with temperature for a typical n-type thermoelectric semiconductor material.

3. Holistic modeling of the TEM performance, results, and discussions

The geometry of the thermoelectric generator is described in the following Fig. 3. The semiconductor legs are assumed to have dimensions of $1.5 \times 1.5 \times 2 \text{ mm}^3$. Space between two legs is 1 mm. Metal inter-connector and electrodes are assumed to have thickness of 0.1 mm. Both the open circuit and close circuit conditions are simulated. The resistor is assumed to be $1.5 \times 1.5 \times 0.1 \text{ mm}^3$ when the thermoelectric generator powers a load.

Properties of semiconductor materials are described as temperature dependent. The Seebeck coefficient of n-type material is assumed to follow Eq. (30). For simplicity, we assume that the Seebeck coefficient of p-type material has the opposite sign of n-type, nevertheless, more complex material properties can be easily incorporated. The electrical conductivity and thermal conductivity of both p-type and n-type are assumed to be equal and follow Eqs. (31) and (32), respectively. The temperature dependences of these parameters can also be referred to as Fig. 4. Other material parameters of the semiconductor are listed in Table 2.

$$\begin{aligned} \alpha &= 348.98 - 1.855T + 0.0061604T^2 - 6.4013 \times 10^{-6}T^3 \\ &\quad + 2.1847 \times 10^{-9}T^4 \quad \mu\text{V/K} \end{aligned} \quad (30)$$

$$\sigma = 70 \times (116.83 + 13561e^{-0.0068336T}) \quad \text{S/cm} \quad (31)$$

$$\kappa = 0.23912 + \frac{609.95}{T} - \frac{838.3}{T^2} \quad \text{W/(m K)} \quad (32)$$

Material properties of the metal inter-connector, electrodes, and wires are defined as constants as following: the Seebeck coefficient is $-3.5 \mu\text{V/K}$; the electrical resistivity is $28.2 \text{ n}\Omega \text{ m}$; the thermal conductivity is 205 W/(m K) ; the heat capacity is 0.897 J/(g K) ; and the density is 2.7 g/cm^3 .

Table 1
Expressions of E_F and $\delta \alpha$ under different temperature levels for n-type material.

		Low-temperature weak-ionization region	Room-temperature strong-ionization region	High-temperature intrinsic-ionization region
n-Type	E_F	$\frac{E_C + E_D}{2} + \frac{k_0 T}{2} \ln \left(\frac{N_D}{2N_C} \right)$	$E_C + k_0 T \ln \left(\frac{N_D}{N_C} \right)$	$\frac{E_C + E_V}{2} + \frac{k_0 T}{2} \ln \left(\frac{N_V}{N_C} \right)$
	$\delta \alpha$	$\frac{k_0}{2e} \left[\ln \left(\frac{N_D}{2N_C} \right) - \frac{3}{2} \right]$	$\frac{k_0}{e} \left[\ln \left(\frac{N_D}{N_C} \right) - \frac{3}{2} \right]$	$\frac{3k_0}{4e} \ln \left(\frac{m_p^*}{m_n^*} \right)$
p-Type	E_F	$\frac{E_V + E_A}{2} - \frac{k_0 T}{2} \ln \left(\frac{N_A}{2N_V} \right)$	$E_V - k_0 T \ln \left(\frac{N_A}{N_V} \right)$	$\frac{E_C + E_V}{2} + \frac{k_0 T}{2} \ln \left(\frac{N_V}{N_C} \right)$
	$\delta \alpha$	$\frac{k_0}{2e} \left[\ln \left(\frac{N_A}{2N_V} \right) - \frac{3}{2} \right]$	$\frac{k_0}{e} \left[\ln \left(\frac{N_A}{N_V} \right) - \frac{3}{2} \right]$	$-\frac{3k_0}{4e} \ln \left(\frac{m_p^*}{m_n^*} \right)$

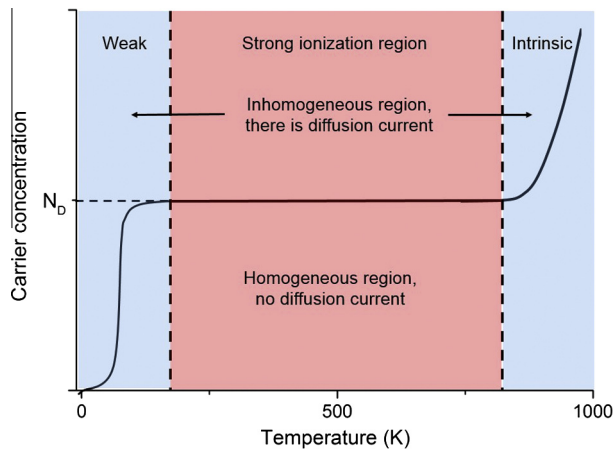


Fig. 2. Rough relationship between carrier concentration and temperature in semiconductor thermoelectric material impurity.

Finite element tool COMSOL® is utilized to develop the model and solve the PDEs numerically. Coefficient form PDE modules are used to describe the governing equations and boundary conditions. Auxiliary equations are imported as functions. The shape of elements are triangle on each surface and thus in tetrahedron shape in three dimensions. Each node has one degree of freedom for temperature, one degree of freedom for voltage potential and three degrees of freedom for current. A grid sensitivity analysis is performed on the sensitivity of results on the size of FEM mesh. The results of four different FEM mesh options are compared. The simulation case is a TEM working under open circuit condition. The overall output voltages are monitored when the bottom surface temperature of the TEM is kept at 340 K and the upper surface temperature ranges from 300 K to 330 K. The results are summarized in Table 3. Physics-controlled fine mesh is selected in the subsequent simulations based on a comprehensive consideration of accuracy and computational time.

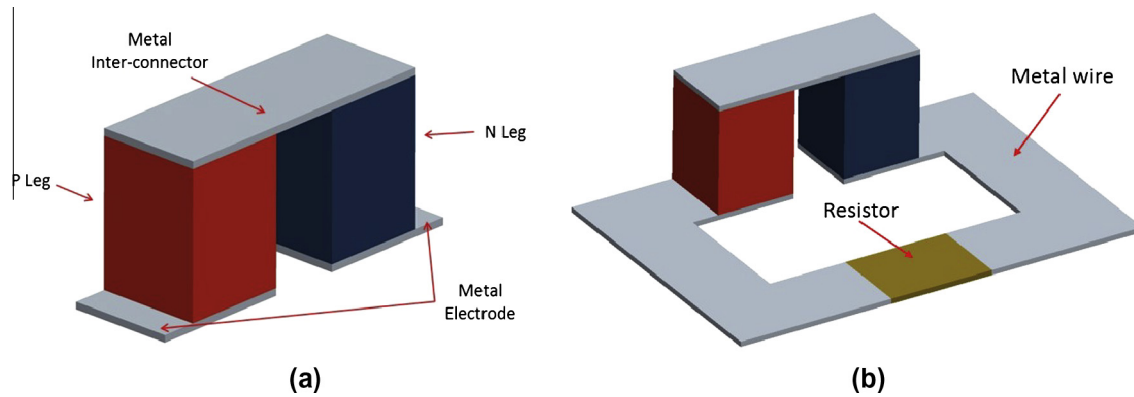


Fig. 3. Geometry of the thermoelectric generator (a) open circuit (b) with a load resistor.

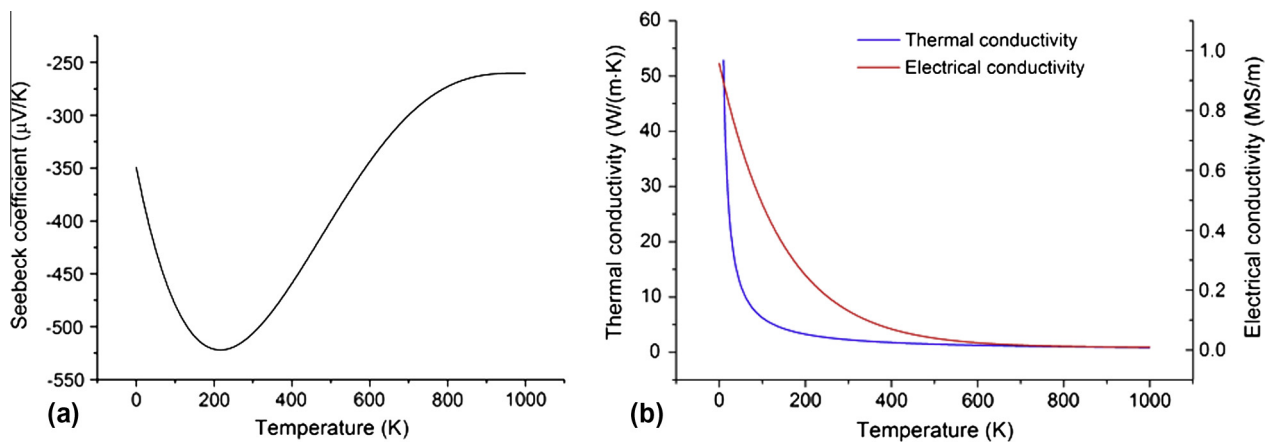


Fig. 4. Temperature dependence of material properties (a) Seebeck coefficient of n-type material (b) electrical conductivity and thermal conductivity.

Table 2
Material properties of semiconductor thermoelectric material.

Parameter	Symbol	Value	Unit	Parameter	Symbol	Value	Unit
Density	ρ_m	7.7	g/cm ³	Heat capacity	C_m	0.1625	J/(g·K)
Electron effective mass	m_n^*	$0.4m_0$	kg	Hole effective mass	m_p^*	$1.1m_0$	kg
Bottom edge of conduction band	E_C	0.67	eV	Top edge of valence band	E_V	0	eV
Energy level for donors	E_D	0.66	eV	Energy level for acceptors	E_A	0.1	eV
Donor impurity concentration	N_D	5×10^{18}	cm ⁻³	Acceptor impurity concentration	N_A	5×10^{18}	cm ⁻³

Table 3

Grid sensitivity test when the TEM is in open circuit.

Open circuit overall output voltage		Finer mesh	Fine mesh	Normal mesh	Coarse mesh
	300 K	4.96 mV	4.96 mV	4.95 mV	4.95 mV
Upper surface temperature	310 K	2.84 mV	2.84 mV	2.84 mV	2.83 mV
	320 K	1.29 mV	1.29 mV	1.29 mV	1.29 mV
	330 K	333.429 μ V	333.722 μ V	334.396 μ V	335.051 μ V
Approximate computation time		110 s	74 s	62 s	51 s

3.1. Behaviors of TEM unit under strong-ionization region

Most thermoelectric power generator are designed to work under strong ionization region which corresponds to the highest ZT value. As methodologies for analyzing TEM performance under weak, strong, and intrinsic ionization regions are similar, the strong-ionization case is firstly presented as an example. Comparisons between different ionization regions are then presented.

For the strong-ionization case, the bottom boundaries of both p-leg and n-leg are set at 340 K. Meanwhile the left side boundary of the bottom left metal electrode is set at potential of 0 V, referring to Fig. 3. The side boundaries of all solid domains are assumed to have convective heat exchange with the ambient, following Eq. (33).

$$-\mathbf{n} \cdot (\kappa \nabla T) = \kappa_c (T_{bottom} - 5 - T) \quad (33)$$

where \mathbf{n} is the outward unit normal vector seen from the inside of a certain solid domain; T_{bottom} is the bottom boundary temperature and T is the temperature at the solid boundary. Eq. (33) means the ambient temperature is assumed to be $T_{bottom} - 5$ and the convective heat transfer coefficient κ_c between the ambient and the module is assumed to be $10 \text{ W}/(\text{m}^2 \text{ K})$. When the environment temperature is higher than the boundary temperature, heat is absorbed into the module. When the environment temperature is lower than the boundary temperature, heat flux flows outwards as seen from the solid domain.

3.1.1. Open circuit

Fig. 5 shows the directions of current driven by Seebeck effect caused e-field and delta Seebeck effect caused e-field when the thermoelectric generator works under 10 K temperature gradient in the strong-ionization region (temperatures at the top surface and bottom surface of the TEM metal electrode are 330 K and 340 K respectively).

Under this temperature range, the Seebeck coefficients of the p-type material and n-type material are positive and negative respectively. Seebeck coefficient is defined as the following equation,

$$\alpha = -\frac{\Delta V_{\text{Seebeck}}}{\Delta T} \quad (34)$$

which means that the temperature gradient is in the opposite direction of the Seebeck caused e-field for positive Seebeck coefficient and it is reverse for negative Seebeck coefficient. As the temperature gradient goes downwards for both p-leg and n-leg, e-field caused by Seebeck effect points upwards in the p-leg and downwards in the n-leg, as is shown in Fig. 5a. It has been pointed out in the early context that the delta Seebeck coefficient has the opposite sign of Seebeck coefficient in strong-ionization region, for both p-type material and n-type material. Whence the e-field induced by the delta Seebeck coefficient is reverse to Seebeck e-field, as shown in Fig. 5b. Under the material property definition of the TEM analyzed here, the absolute value of delta Seebeck coefficient is much smaller than the Seebeck coefficient, so the overall effective Seebeck e-field is still in the same direction of the Seebeck e-field, as shown in Fig. 5c.

Fig. 6 illustrates the directions of current driven by voltage-potential-induced e-field and carrier density gradient. The total current is the superposition of those current components, based on Eq. (9). For TEM with evenly doped impurities and working under strong-ionization condition, the carrier density is constant everywhere according to Eq. (29). This results in a zero net diffusion current density as shown in Fig. 6b. Driven by the effective Seebeck e-field, current flows from the p-leg to the n-leg, as shown in Fig. 6c. A positive voltage potential forms at the right side of the bottom right metal electrode, which cause a reverse voltage potential through the TEM, as depicted in Fig. 6a.

Fig. 7 presents the distributions of temperature, current density, and voltage inside the thermoelectric module. Fig. 7a shows that the temperature changes from 330 K to 340 K gradually from top surface to bottom surface. Eq. (3) used in the simulation model (i.e., $\nabla \cdot \mathbf{J} = 0$), implies that there is no current source or sink inside the module. It forces all carriers in the semiconductor legs to flow through the metal inner-connector. Fig. 7b shows that the current magnitude is much higher in the top metal inner-connector. Meanwhile the current amplitude remains relatively stable specifically

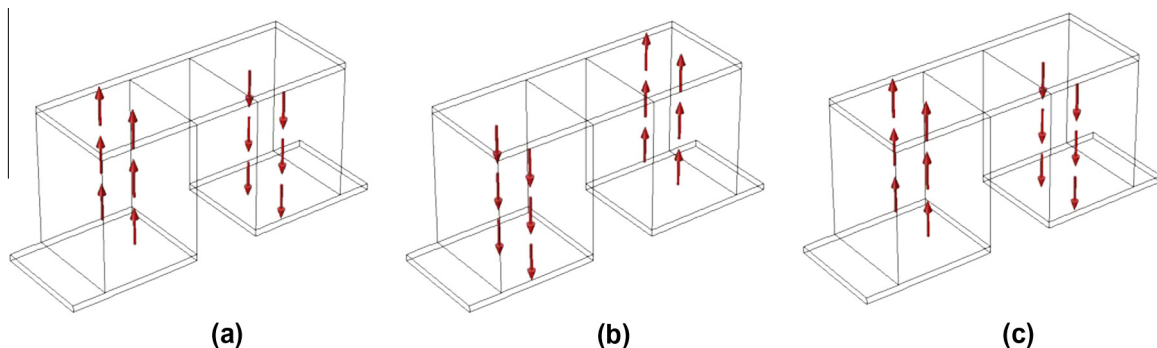


Fig. 5. Directions of current driven by (a) Seebeck e-field (b) delta Seebeck e-field and (c) effective Seebeck e-field when the thermoelectric generator is working under 10 K temperature difference and in open circuit (arrows only illustrate the direction of current, not their magnitudes).

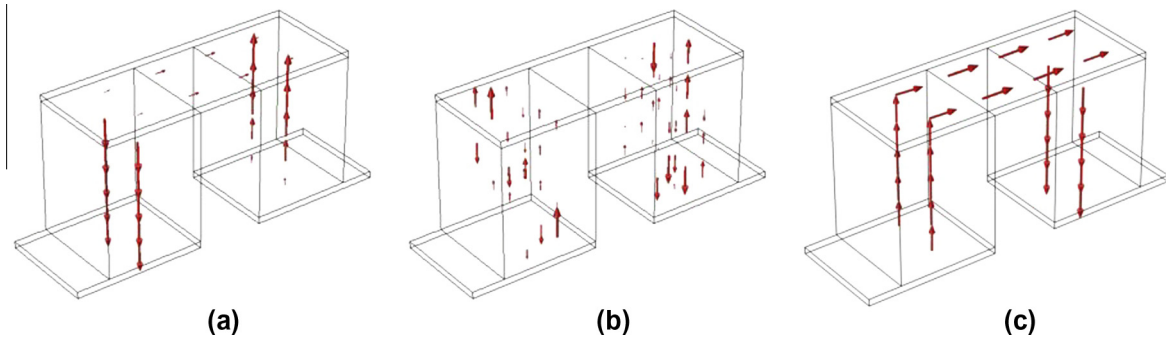


Fig. 6. Directions of current driven by (a) voltage potential e-field, (b) carrier density gradient and (c) the total current direction, when the thermoelectric generator is working under 10 K temperature difference and in open circuit (arrows only illustrate the direction of current, not magnitudes).

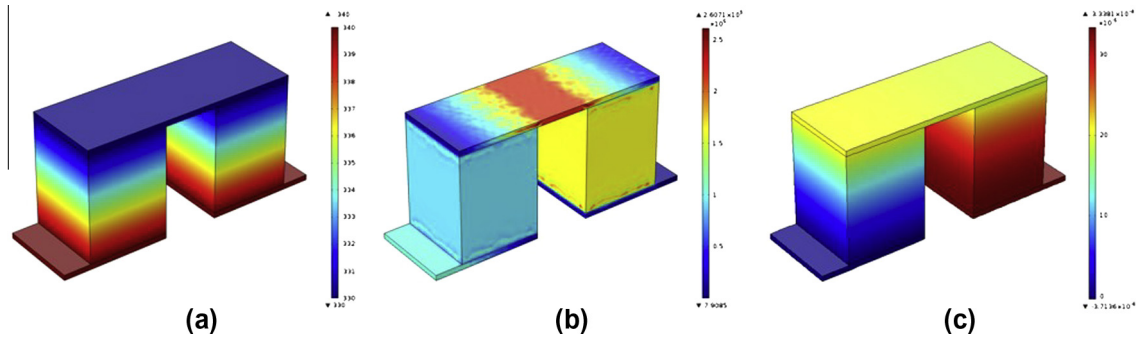


Fig. 7. Distribution of (a) temperature (b) current density and (c) voltage when the thermoelectric generator is working under 10 K temperature difference and in open circuit.

for the p-leg and n-leg. Fig. 7c proves that the output voltage is positive when temperature gradient is going upwards.

When the temperature of top boundary of the metal inter-connector is swept from 300 K to 340 K, while the temperature of the bottom boundary of the metal electrodes remain at 340 K, the one dimensional temperature, current density amplitude, Thomson heat and voltage distribution along the middle line of p-leg and n-leg (also including the bottom metal electrodes and top metal inner-connector) are shown in Fig. 8 respectively. The part from 0 to 0.1 mm along the horizontal axis corresponds to the bottom metal electrodes. The part from 0.1 mm to 2.1 mm corresponds to the p-leg or n-leg. The part from 2.1 mm to 2.2 mm corresponds to the top metal inner-connector.

From the material properties definitions of the TEM used in this simulation, $m_p^* > m_n^*$. So $N_V > N_C$ according to Eq. (29). Considering $N_A = N_D$ here, so we know that the absolute value of delta Seebeck coefficient of the p-leg is larger than n-leg, based on parameters listed in Table 1. Therefore, the absolute value of effective Seebeck coefficient of the p-leg is smaller than n-leg, which results in that the current density amplitude of the p-leg is smaller than that of n-leg, as shown in Fig. 8b.

The Thomson heat by the semiconductor material is $-TJ[(\frac{\partial \alpha}{\partial T})\nabla T + (\nabla \alpha)_T]$, according to Eq. (2). In the temperature range corresponding to strong-ionization region, $\frac{\partial \alpha}{\partial T}$ is negative for p-leg and positive for n-leg. Because J and ∇T have the opposite direction in p-leg and the same direction in n-leg, the Thomson heat term is negative for both p-leg and n-leg, which means that heat is extracted from the semiconductor material. The higher the current density, the more heat is extracted. Fig. 8c verifies the prediction, where Thomson heat is negative for both n-leg and p-leg and n-leg absorbs more Thomson heat. It can also be noticed that there is a jump in the absorbed heat around the junctions between semiconductor legs and the metal electrodes. This is possibly due to the Peltier heat change in addition to the Thomson heat.

Even though n-leg has a higher current density than p-leg (which leads to a higher heat loss of the n-leg), the temperature distributions of p-leg and n-leg are approximately the same, seen from Fig. 8a. This is because more Joule heat is produced inside the n-leg, which compensates its relatively higher heat loss.

Fig. 8d shows the open circuit voltage potential distributions under different temperature differences, where the dash line values are the overall output voltage of the module. It implies that the relationship between the output voltage and the temperature difference across the TEM is nonlinear. The larger the temperature difference, the higher the slope of the output voltage versus temperature difference curve, i.e., the higher the effective Seebeck coefficient.

3.1.2. TEM performance with a resistive load

Simulations are also conducted when the TEM is powering an electric load (i.e., a resistor), with set up as shown in Fig. 3b. The resistivity of the load resistor is swept from 10^{-8} to $10^{-3} \Omega m$, approximately ranging from short circuit to open circuit conditions. The output current and output voltage are shown in Fig. 9a as functions of load resistance. The output power is obtained from the output current and voltage. The output power efficiency is determined by further dividing the absorbed heat from the bottom boundary of the TEM. The variations of absorbed heat and the output power efficiency with load resistance are shown in Fig. 9b.

Fig. 9 implies that output current decreases and output voltage increases as load resistivity goes up. The absorbed heat, however, does not change much as load resistance changes. The maximum output power efficiency occurs at resistivity of round $1 \mu\Omega m$ (or output resistance of 0.01Ω), which corresponds to the point that the load resistance is equal to the inner resistance of the TEM. Results of the simulations here indicate that the larger the temperature difference across the TEM element, the larger the output

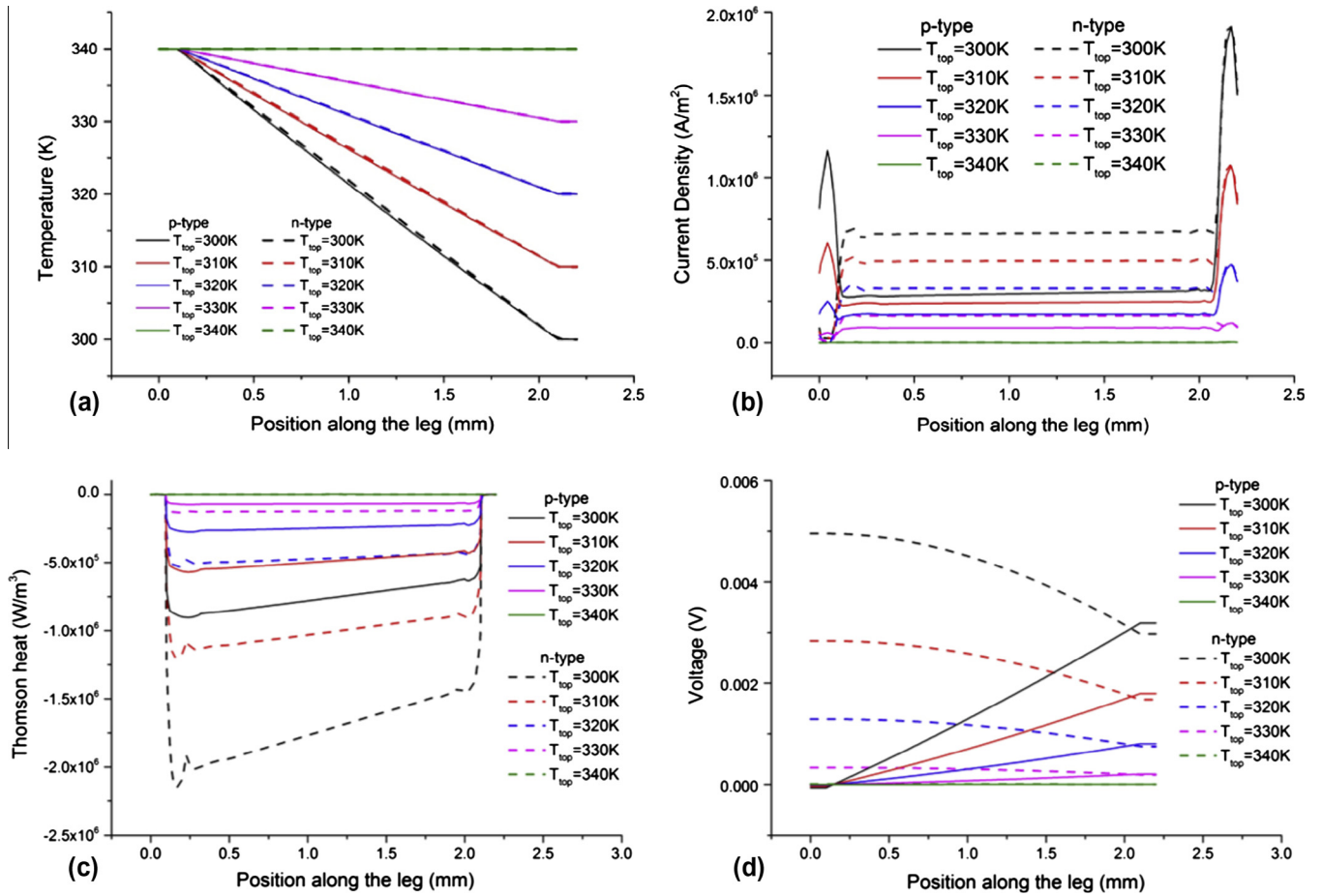


Fig. 8. One dimensional distributions of (a) temperature (b) current density amplitude (c) absorbed Thomson heat and (d) voltage, along the middle line of p-leg and n-leg.

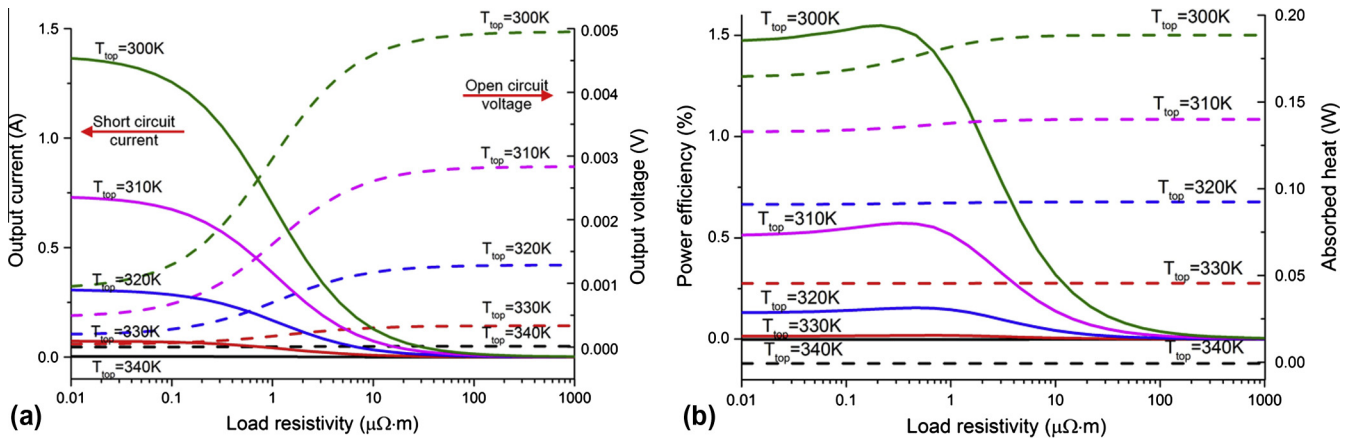


Fig. 9. (a) Functions of output current and output voltage with respect to different load resistivity (solid lines represent output current. Dash lines represent output voltage. Red arrows means when the load resistivity goes down to $10^{-8} \Omega \text{ m}$, the circuit is similar to a short circuit condition. When the load resistivity goes up to $10^{-3} \Omega \text{ m}$, the circuit approaches to the open circuit condition); (b) monitored absorbed heat from the bottom boundary of the TEM and the output power efficiency as functions of load resistivity (solid lines correspond to power efficiency. Dash lines correspond to absorbed heat). (For interpretation of the references to colour in this figure legend, the reader is referred to the web version of this article.)

power and power efficiency, which are consistent with general observations in TEM.

3.2. Behaviors of TEM unit working under different ionization regions predicted by the new model versus traditional model

Simulations are also conducted when TEM unit works under weak-ionization region, strong-ionization region, and intrinsic-

ionization region. For all these conditions, temperature difference of 10 K is assumed across the TEM element. The reference temperature at the bottom conductor are 140 K, 340 K, and 1000 K respectively. The same boundary conductive heat exchange is assumed (Eq. (33)). Computational simulations based on traditional model following Eq. (1) are also conducted as references under corresponding temperature conditions (which are plotted in dash lines).

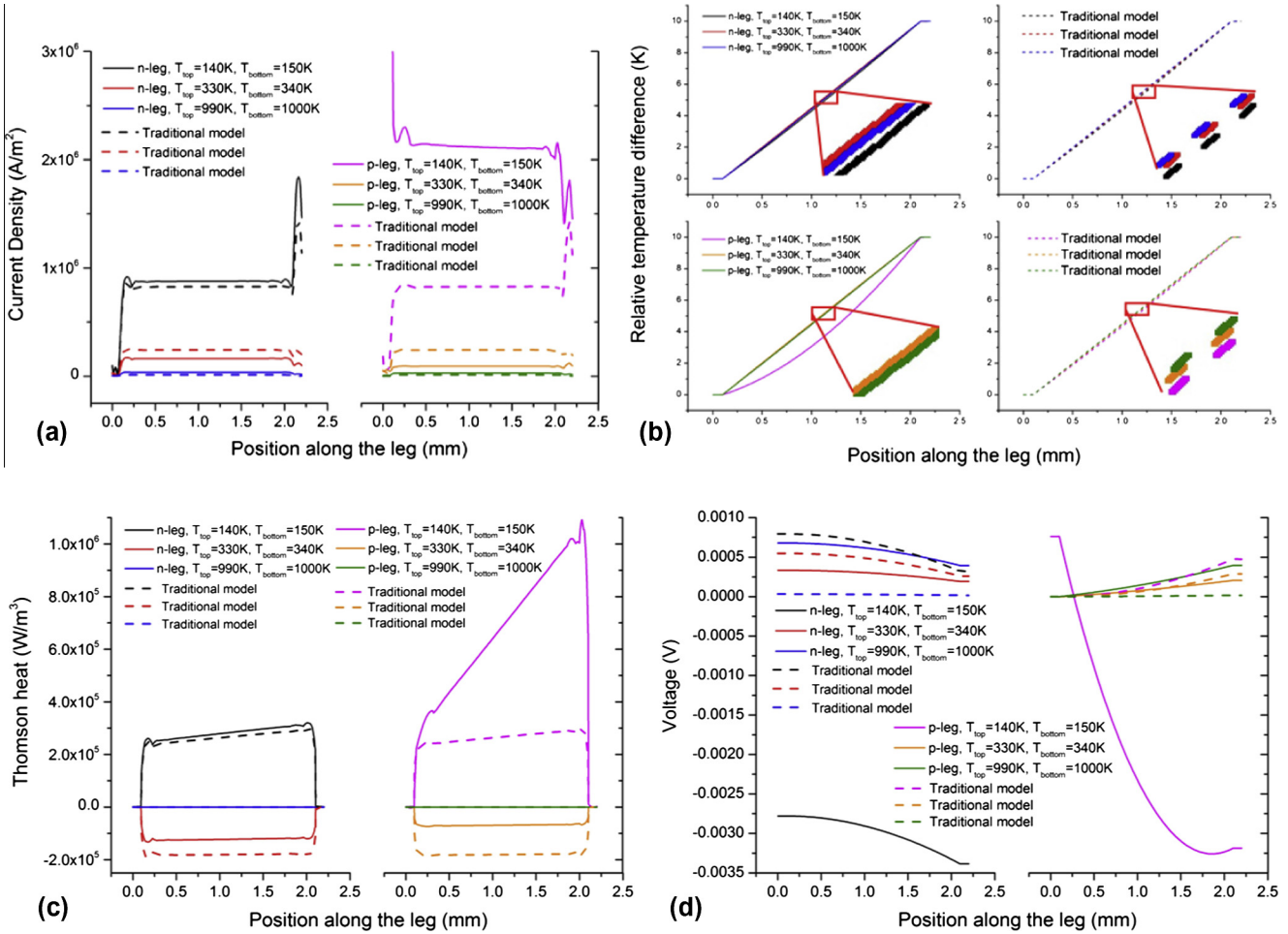


Fig. 10. Open circuit thermoelectric power generator performances comparison between different ionization regions when the TEM is working under 10 K temperature difference, with traditional model results as references, including one dimensional distributions of (a) current density amplitude, (b) temperature (portion of the curves are zoomed in), (c) absorbed Thomson heat, (d) voltage potential.

Fig. 10a shows that when working under weak-ionization region, the current amplitude is much bigger in the bottom left metal electrode than anywhere else, while traditional model does not predict this behavior. For weak and intrinsic ionization regions, the new model predicted higher current densities than the traditional model by 6% and 195%. This is due to the big diffusion current under inhomogeneous conditions that is captured by this model. In strong-ionization region, the new model predicts a 32% smaller current density than the traditional model, because the delta Seebeck coefficient is opposite to that of the Seebeck effect under strong-ionization region. It can also be seen from the figure that under the same temperature difference, the higher the working temperature of the module, the lower the current density amplitude. This result is possibly due to the fact that the electrical conductivity of a material decreases with increasing temperature.

Fig. 10b shows the change of the relative temperature difference along the p-leg and n-leg. The relative temperature difference is calculated as the absolute value of the temperature at a certain point minus the bottom boundary temperature. The figure indicates that the relative temperature differences are approximately the same under various conditions. The only remarkable phenomena appears for the case of the relative temperature difference at p-leg under weak-ionization condition, which is lower than the conditions. It means the temperature inside the p-leg is relative lower than under other conditions. Referring to the material property definitions of the TEM, the term $\frac{\partial \alpha}{\partial T}$ is negative for n-leg and positive for p-leg, which is reverse to the scenario under strong

and intrinsic ionization regions. Consequently, heat is absorbed from the ambient inwards to the semiconductor leg. This explains the relative temperature difference in the p-leg under weak-ionization region is lower than other cases, which can also be proved by Fig. 10c as the Thomson heat for the p-leg under weak-ionization range is significantly larger than those under the other cases. Such effects, however, is not captured by the traditional simulation model.

Fig. 10d plots the voltage distribution in the p-leg and n-leg of the TEM unit under different working conditions. The results imply that the current direction in the p-leg under weak-ionization temperature, which goes from bottom to top, is opposite to those in all the other cases where the current goes from top to bottom. Due to the large magnitude produced voltage in the p-leg, the resultant overall output voltage of the module is negative. Another important observation from this figure is that the traditional simulation model implies under the same temperature difference of 10 K, the higher the working temperature of the module, the lower the output voltage. However, the new model predicts a reverse trend. The results of the new model indicates that as the working temperature increases, the absolute value of the output voltage will first decrease and then increase. For temperatures in the strong-ionization region, the voltage output predicted by the new model is 39% lower than that predicted by the traditional model.

Results for the case with a load resistor are shown in Fig. 11a and b. The absolute value of output current decreases and output voltage increases when load resistivity increases. The resistivity

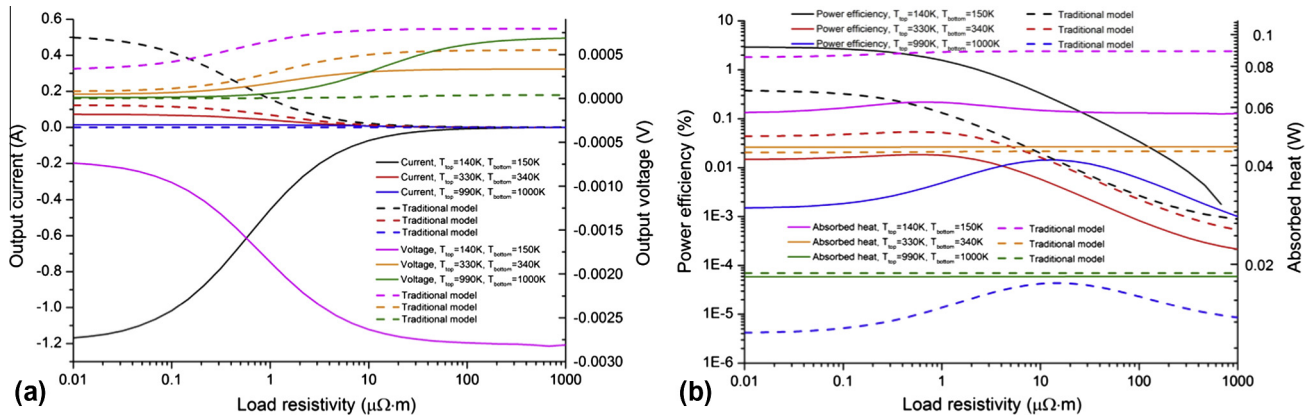


Fig. 11. Close circuit TEM performance comparison between different ionization regions when TEM is working under 10 K temperature difference, with traditional model results as references (a) output voltage and current as functions of load resistivity; (b) absorbed heat and output power efficiency as functions of load resistivity.

corresponding to the maximum output power efficiency increases as the temperature of the TEM increases. It is about $0.01 \mu\Omega\cdot m$, $1 \mu\Omega\cdot m$ and $10 \mu\Omega\cdot m$ for the weak, strong, and intrinsic ionization regions, respectively. This might be related to the increases in the electrical resistance of TEM materials with temperature. For the strong-ionization region, the maximum output power efficiency predicted by the new model predicts is 65% lower than the traditional model. Meanwhile the output current and voltage corresponding to the maximum power efficiency working point predicted by the new model are lower than the traditional model prediction. This is because that the delta Seebeck coefficient is opposite to that of the Seebeck effect when working under temperature in the strong-ionization region.

4. Conclusion

This paper describes the development of the governing equations and auxiliary relationships to implement holistic simulations of TEM behaviors. The thermoelectric processes of Seebeck, Peltier, and Thomson effects and Joule heat are included in the model. Particularly, this model considers the influence of the effective Seebeck coefficient and the carrier concentration variations. Different working temperature regions corresponding to transitions in carrier concentrations are also considered. Finite element simulations are conducted on a thermoelectric generator unit under the open and close circuit conditions.

For the open circuit scenario, the physics phenomena inside the thermoelectric module during thermoelectric generation process are discussed. In order to analyze the movements of the carriers inside the thermoelectric power generator, current driven by the thermal gradient is decomposed into components driven by Seebeck e-field, delta Seebeck e-field, effective Seebeck e-field, voltage potential e-field and carrier density gradient, respectively. Comparison indicates that the carrier movements are mainly decided by the Seebeck effect induced electric field, even though they are impaired by the effective Seebeck effect and the output voltage induced electric field. The carrier movements because of carrier density variation under strong-ionization region does not play a major role when the thermoelectric legs are evenly doped. However, they have significant contribution to the overall current when working under weak and intrinsic ionization regions. This proves that the density variations of carriers on the performance of TEM generator cannot be neglected. The overall temperature, current density, Thomson heat and voltage potential distributions are described. The results indicate that the relationship between the output voltage and the temperature difference across the thermoelectric power generator is non-linear, partly due to the

effects of temperature dependency of thermoelectric material properties.

For the close circuit scenario with a load resistor, simulation results on the power performances of the thermoelectric power generator are discussed. The performance of the TEM at different temperature ranges (corresponding to different ionization regions) are compared. Results of traditional model are introduced as the reference base. The output voltage, current, absorbed heat and power efficiency are described. The power generator works at its best efficiency when the load resistance equals to the inner resistance. The results show that the effective Seebeck coefficient and the carrier concentration variations have significant influences on the performance of the TEM elements. When the thermoelectric power generator is working under strong-ionization region, the output voltage, current and output power efficiency predicted by the new model is lower than those predicted by the traditional model. As the traditional model has been proved to overestimates the performance of the power generator under strong-ionization region [29], it implies that the new model has the potential to describe the TEM behaviors more precisely. The results also show that ignoring the effects of effective Seebeck coefficient (delta Seebeck coefficient) and carrier concentration variations as commonly done in the traditional simulations models fails to capture many unique behaviors of TEM module.

This holistic simulation model provides important tool to assist the design optimization and performance prediction of innovative TEM applications.

Acknowledgements

Research presented in this paper is partially supported by the U.S. National Science Foundation via projects CMMI 0846475 and CMMI 1300149. These support are highly appreciated.

References

- [1] Leonov V, Fiorini P, Sedky S, Torfs T, Van Hoof C. Thermoelectric MEMS generators as a power supply for a body area network. In: The 13th international conference on solid-state sensors, actuators and microsystems, 2005, vol. 1. Digest of technical papers. TRANSDUCERS'05; 2005. p. 291–4.
- [2] Saqr KM, Mansour MK, Musa M. Thermal design of automobile exhaust based thermoelectric generators: objectives and challenges. *Int J Automot Technol* 2008;9:155–60.
- [3] Wu G, Yu XB. Thermal energy harvesting system to harvest thermal energy across pavement structure. *Int J Pavement Res Technol* 2012;5:311–6.
- [4] Heng X, Xiaolong G, Chen Y. Simulation analysis on thermoelectric generator system performance. In: Asia simulation conference – 7th international conference on system simulation and scientific computing, 2008. ICSC 2008; 2008. p. 1183–7.

- [5] Bahk J-H, Youngs M, Yazawa K, Shakouri A, Pantchenko O. An online simulator for thermoelectric cooling and power generation. In: *Frontiers in education conference*, 2013. IEEE; 2013. p. 1757–9.
- [6] Heikes RR, Ure RW. *Thermoelectricity: science and engineering*. New York: Interscience Publishers; 1961.
- [7] Junior C, Richter C, Tegethoff W, Lemke N, Köhler J. Modeling and simulation of a thermoelectric heat exchanger using the object-oriented library TIL. In: *Proceedings of the 6th international modelica conference*; 2008. p. 437–45.
- [8] Phillip N, Maganga O, Burnham KJ, Dunn J, Rouaud C, Ellis MA, et al. Modelling and simulation of a thermoelectric generator for waste heat energy recovery in low carbon vehicles. In: *2nd International symposium on environment friendly energies and applications (EFEA)*; 2012. p. 94–9.
- [9] Chakraborty A, Saha BB, Koyama S, Ng KC. Thermodynamic modelling of a solid state thermoelectric cooling device: temperature–entropy analysis. *Int J Heat Mass Transfer* 2006;49:3547–54.
- [10] Drabkin L, Ershova L. Comparison of approaches to thermoelectric modules mathematical optimization. In: *25th International conference on thermoelectrics*, 2006. ICT'06; 2006. p. 476–9.
- [11] Wee D. Analysis of thermoelectric energy conversion efficiency with linear and nonlinear temperature dependence in material properties. *Energy Convers Manage* 2011;52:3383–90.
- [12] Sherman B, Heikes RR, Ure RW. Calculation of efficiency of thermoelectric devices. *J Appl Phys* 1960;31:1–16.
- [13] Hoyos GE, Rao KR, Jerger D. Numerical analysis of transient behavior of thermoelectric coolers. *Energy Convers* 1977;17:23–9.
- [14] Lossec M, Multon B, Ben Ahmed H, Goupil C. Thermoelectric generator placed on the human body: system modeling and energy conversion improvements. *Eur Phys J Appl Phys* 2010;52.
- [15] Lineykin S, Ben-Yaakov S. Modeling and analysis of thermoelectric modules. *IEEE Trans Ind Appl* 2007;43:505–12.
- [16] Min C, Junling G, Zhengdong K, Jianzhong Z, Qungui D, Suzuki RO. Design methodology of large-scale thermoelectric generation: a hierarchical modeling approach in SPICE. In: *Industry applications society annual meeting (IAS)*, 2011. IEEE; 2011. p. 1–7.
- [17] Dziurdzia P. Modeling and simulation of thermoelectric energy harvesting processes. *Sustain Energy Harvest Technol Past Present Future* 2011:109–28.
- [18] Chen M, Bach IP, Rosendahl L, Condra T, Pedersen JK. Notes on computational methodology and tools of thermoelectric energy systems. In: *Proceedings of meeting on applied scientific computing and tools*; 2007. p. 213–21.
- [19] Min C, Rosendahl LA, Condra TJ, Pedersen JK. Numerical modeling of thermoelectric generators with varying material properties in a circuit simulator. *IEEE Trans Energy Convers* 2009;24:112–24.
- [20] Gould C, Shammass N, Grainger S, Taylor I. A novel 3D TCAD simulation of a thermoelectric couple configured for thermoelectric power generation. In: *Int conf on renewable energies and power quality*; 2011.
- [21] Gould C, Shammass N, Grainger S, Taylor I. Thermoelectric power generation: properties, application and novel TCAD simulation. In: *Proceedings of the 2011-14th European conference on power electronics and applications (EPE 2011)*; 2011. p. 1–10.
- [22] Gould C, Shammass N. Three dimensional TCAD simulation of a thermoelectric module suitable for use in a thermoelectric energy harvesting system; 2012.
- [23] Gould C, Shammass N, Grainger S, Taylor I, Simpson K. A 3D TCAD simulation of a thermoelectric module configured for thermoelectric power generation, cooling and heating. In: *AIP conference proceedings*; 2012. p. 65.
- [24] Antonova EE, Looman DC. Finite elements for thermoelectric device analysis in ANSYS. In: *24th International conference on thermoelectrics*, 2005. ICT 2005; 2005. p. 215–8.
- [25] Saber HH, El-Genk MS. A three-dimensional, performance model of segmented thermoelectric converters. *AIP Conf Proc* 2002;608:998–1006.
- [26] Jaegle M. Multiphysics simulation of thermoelectric systems-modeling of Peltier-cooling and thermoelectric generation. In: *COMSOL conference 2008*, Hannover; 2008.
- [27] Topal ET. A flow induced vertical thermoelectric generator and its simulation using COMSOL multiphysics. In: *Proceedings of the 2011 COMSOL conference*, Boston, MA; 2011.
- [28] Martin J. Computational Seebeck coefficient measurement simulations. *J Res (NIST JRES)* 2012;2:2.
- [29] Ebling D, Jaegle M, Bartel M, Jacquot A, Böttner H. Multiphysics simulation of thermoelectric systems for comparison with experimental device performance. *J Electron Mater* 2009;38:1456–61.
- [30] Chen M, Rosendahl LA, Condra T. A three-dimensional numerical model of thermoelectric generators in fluid power systems. *Int J Heat Mass Transfer* 2011;54:345–55.
- [31] Bistschi A. Modelling of thermoelectric devices for electric power generation. Phd Dissertation, Swiss Federal Institute of Technology; 2009.
- [32] Wagner M. Simulation of thermoelectric devices; 2007.
- [33] Fraisse G, Ramousse J, Sgorlon D, Goupil C. Comparison of different modeling approaches for thermoelectric elements. *Energy Convers Manage* 2013;65:351–6.
- [34] Turenne S, Clin T, Vasilevskiy D, Masut RA. Finite element thermomechanical modeling of large area thermoelectric generators based on bismuth telluride alloys. *J Electron Mater* 39:1926–33. 2010/09/01 2010.
- [35] Picard M, Turenne S, Vasilevskiy D, Masut RA. Numerical simulation of performance and thermomechanical behavior of thermoelectric modules with segmented bismuth-telluride-based legs. *J Electron Mater* 42:2343–9. 2013/07/01 2013.
- [36] Mahan GD. Density variations in thermoelectrics. *J Appl Phys* 2000;87:7326–32.
- [37] Rowe DM. *Thermoelectrics handbook: macro to nano*. CRC Press; 2006.
- [38] Harman TC, Honig JM. *Thermoelectric and thermomagnetic effects and applications*. New York: McGraw-Hill; 1967.
- [39] Barnard RD. *Thermoelectricity in metals and alloys*. London: Taylor & Francis; 1972.
- [40] Enke L, Bingsheng Z, Jinsheng L. *Semiconductor physics*. Beijing: Publishing House of Electronics Industry; 2003.